

Towards multi-variable tsunami damage modeling for coastal roads: Insights from the application of explainable machine learning to the 2011 Great East Japan Event

Mario Di Bacco^a, James H. Williams^b, Daisuke Sugawara^c, Anna Rita Scorzini^{d,*}

^a Department of Civil and Environmental Engineering, University of Florence, Firenze, 50139, Italy

^b School of Earth and Environment, University of Canterbury, Christchurch, 8041, New Zealand

^c International Research Institute of Disaster Science, IRIDeS, Tohoku University, Sendai, 980-8572, Japan

^d Department of Civil, Environmental and Architectural Engineering, University of L'Aquila, L'Aquila, 67100, Italy

ARTICLE INFO

Keywords:

Road
Damage
Tsunami
Machine learning
Multi-variable
Fragility function
Uncertainty

ABSTRACT

The accurate assessment of tsunami-induced damage to coastal roads is crucial for effective disaster risk management. Traditional approaches, reliant on univariate fragility functions, often fail to capture the complex interplay of variables influencing road damage during tsunami events. This study addresses this limitation by employing machine learning techniques on an extensive dataset compiled after the 2011 Great East Japan tsunami. The dataset, enriched with additional explicative variables accounting for the hydraulic features of the event and the physical characteristics at roads' location, enables a comprehensive analysis of road damage mechanisms. Results indicate that while inundation depth remains a significant predictor, factors such as wave approach angle, road orientation and potential overflow from inland watercourses also play critical roles.

1. Introduction

The accurate estimation of tsunami-induced damage to roads poses a challenge for disaster risk management in coastal areas, emphasizing the need for comprehensive approaches and tools to assess and mitigate tsunami impacts on roads (Ballantyne, 2006; Edwards, 2006; Tang et al., 2006; Fritz et al., 2011; Kazama & Noda, 2012; Unjoh, 2012; Williams et al., 2019, 2020; Paulik et al., 2021). Roads, integral to the daily functioning of society, assume a critical role during response and recovery phases following major events. Indeed, as observed in past events (e.g., 2004 Indian Ocean tsunami, 2011 Great East Japan tsunami, 2015 Illapel tsunami in Chile), beyond merely facilitating access to impacted communities, road integrity considerably influences the efficiency of repair works on other essential lifelines (e.g., electricity, telecommunications), each with a widespread damage and loss of service to transportation.

While some literature and practical approaches exist for modeling flood-induced direct damage to roads (Davis et al., 2013; Mallick et al., 2017; Rebally et al., 2021; Van Ginkel et al., 2021; Haque et al., 2023; Samela et al., 2023), similar methodologies have not received an

equivalent attention for tsunamis. Due to the limited availability of specific empirical data for model development and validation, prevailing literature for tsunamis has primarily focused on developing modeling tools for buildings (Tarbotton et al., 2015; Charvet et al., 2017). In the few examples existing for roads, the most frequent approach involves the use of fragility functions (Maruyama & Itagaki, 2017; Williams et al., 2020), which establish a relationship between the damage state and the hazard intensity, typically represented by tsunami inundation depth (Koshimura et al., 2009). While practical, relying on inundation depth as the sole hazard intensity measure represents a principal drawback of fragility functions, due to their inability to fully capture the complex mechanisms leading to damage (Vescovo et al., 2023; Scorzini et al., 2024). Morphological attributes of roads and their surrounding environment, coupled with factors like flow velocity, entrained debris and erosion, are known as significant influencing factors for road damage (Ratnasooriya et al., 2007; Rossetto et al., 2007; Kreibich et al., 2009; Mikami et al., 2012; Chen et al., 2013; Williams et al., 2019, 2020; Haque et al., 2023). Despite their importance, conventional uni-variable fragility functions often neglect these critical factors and their complex, non-linear interactions, posing a question

* Corresponding author.

E-mail addresses: mario.dibacco@unifi.it (M. Di Bacco), j.williams@canterbury.ac.nz (J.H. Williams), sugawara@irides.tohoku.ac.jp (D. Sugawara), annarita.scorzini@univaq.it (A.R. Scorzini).

<https://doi.org/10.1016/j.scs.2024.105856>

Received 5 May 2024; Received in revised form 25 September 2024; Accepted 26 September 2024

Available online 27 September 2024

2210-6707/© 2024 The Author(s). Published by Elsevier Ltd. This is an open access article under the CC BY-NC-ND license (<http://creativecommons.org/licenses/by-nc-nd/4.0/>).

regarding the reliability of such tools.

In this context, recent advancements in machine learning present a promising solution to these drawbacks (Di Bacco et al., 2023; Martín-García et al., 2023; Vescovo et al., 2023; Scorzini et al., 2024). Nevertheless, a downside of such approaches is their dependency on extensive empirical datasets to develop effective and generalizable models. In this regard, the road damage dataset compiled by the Japanese Ministry of Land, Infrastructure, Transport and Tourism (MLIT) after the 2011 Tōhoku tsunami may offer a valuable resource (MLIT, 2012). The 2011 Great East Japan earthquake triggered an extremely large tsunami that adversely affected the eastern Pacific Coast of the country, causing casualties and severe damage in coastal cities of Miyagi and Iwate prefectures (Mimura et al., 2011; Kazama & Noda, 2012; Mikami et al., 2012). The MLIT conducted field surveys across the entire tsunami-affected area to gather data on damaged assets, resulting in a comprehensive dataset accessible through their website (MLIT, 2012). While the building dataset has been widely employed in the literature for developing fragility functions (e.g., Tarbotton et al., 2015; Macabuag et al., 2016) and, more recently, machine learning-based models (Di Bacco et al., 2023; Vescovo et al., 2023; Scorzini et al., 2024), the road dataset has received comparably less attention, with only a few studies still relying exclusively on fragility-based approaches (Maruyama & Itagaki, 2017; Williams et al., 2020).

In the present study, the MLIT road dataset has been extended by incorporating supplementary explanatory variables, with the aim of obtaining insights into the multi-variable nature of tsunami damage mechanisms to roads within a machine learning framework. These additional factors include the hydraulic characteristics of the event (inundation depth and flow velocity), the morphological/topographical features at the road location and proxy variables accounting for shielding effects and debris impacts generated by adjacent structures.

2. Materials and methods




2.1. Extended MLIT dataset for roads

The main data source in this study originated from the comprehensive ground survey carried out by the Japanese Ministry of Land, Infrastructure, Transport and Tourism (MLIT) in the weeks following the 2011 Tōhoku tsunami (MLIT, 2012). The dataset comprised a line shapefile representing the actual length of each damaged road segment, with an assigned damage state (Table 1), categorized as “minor” (class 1, ds_1), “moderate” (class 2, ds_2), or “severe” (class 3, ds_3). It also included information on road-use type based on jurisdiction, distinguishing between state roads, main local roads, general prefectural roads, and municipality roads, providing a proxy for road capacity and design level.

In this study, to ensure a comprehensive representation of the road network within the inundated area, the MLIT dataset was combined with the undamaged (ds_0) road layer developed by Williams et al. (2020) using information from OpenStreetMap or digitized from aerial imagery. This integration resulted in approximately 4300 km of inundated roads distributed across four damage states (including the undamaged one), as shown in Fig. 1.

The hydrodynamic data for the event were obtained using TUNAMI-STM, a two-dimensional nonlinear shallow water model coupled with a sediment transport model, whose accuracy and reliability have been tested and documented in previous studies (Sugawara & Goto, 2012; Sugawara et al., 2014; Sugawara, 2018; Yamashita et al., 2016, 2017, 2022). To efficiently manage computational demands, the impacted region was divided into multiple nested domains, labeled as R6-R1, each with distinct spatial resolution and extent. Domains R6 to R2 had resolutions ranging from 5 to 405 m, maintaining a constant ratio of 1/3. Domain R1 extended over the entire interplate tsunami source region along the Japan Trench, with a resolution of 1215 m. Digital elevation models were generated using high-resolution data sources, including pre-2011 tsunami records, LIDAR and photogrammetry provided by the

Table 1
Road damage classification with illustrative examples sourced from MLIT (2012).

Damage state	ds_0	ds_1	ds_2	ds_3
Damage definition	No damage	Minor damage	Moderate damage	Severe damage
Damage description	No damage	Localized minor damage, without significant impact on drivability	Major damage to one road lane, with partial impact on drivability	Complete destruction of the roadway or extensive damage affecting most of the lanes, rendering travel impossible
Illustrative example				

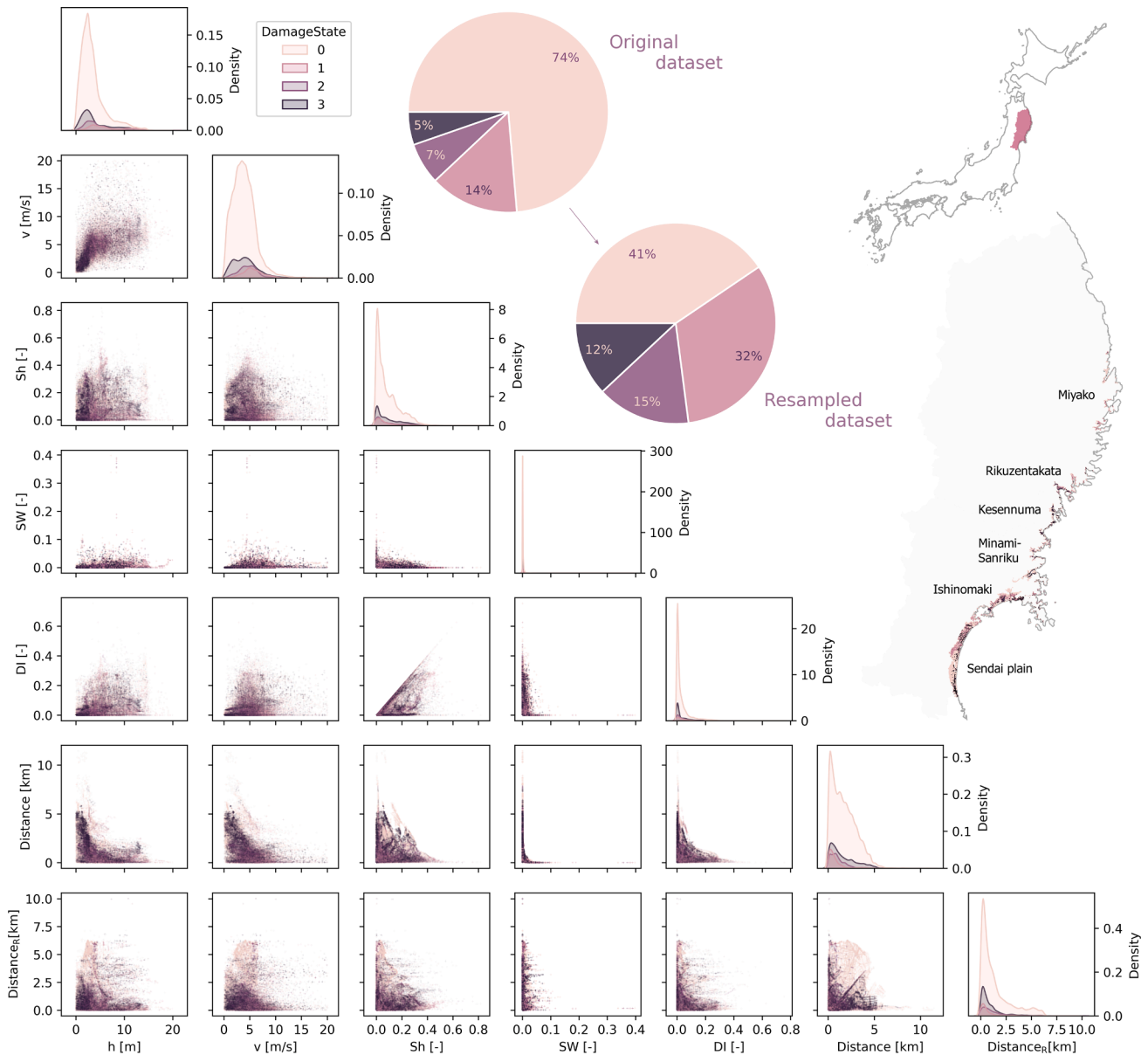


Fig. 1. Pairwise relationships between hazard, main velocity proxies and distance variables across the damage states in the extended MLIT dataset for roads. The definitions of the variables are provided in Table 2. The pie chart summarizes the distribution of the various damage states within the original and resampled datasets, including respectively 129,557 and 57,454 items.

Geospatial Information Authority of Japan. To enhance model’s accuracy and minimize uncertainties from coarser grid sizes, our analysis specifically focused on roads within Regions R6-R4, covering approximately 3790 km of inundated roads. The investigated region included the coastal areas of Miyako, Rikuzentakata, Kesennuma, Minami-Sanriku, Ishinomaki and Sendai plain (Fig. 1). Simulations reproduced the tsunami’s propagation and inundation over a 3-hour period following the earthquake, capturing both the primary wave and subsequent backflow effects.

Roads in the inundated area were divided into segments of approximately 50 m. At each segment’s centroid, corresponding attributes were assigned, including simulated values for inundation depth (h) and flow velocity (v) obtained through grid sampling. The sampled values at these locations represent the maximum estimated values from the numerical simulation, thus implying that observed damage is triggered by overall maximum demands, regardless of the potential variation in the timing of occurrence for the maximum depth and velocity at a given location.

Beyond hazard information, to gain more insights into the multi-

variable nature of tsunami damage, geospatial algorithms were employed to characterize each road segment with additional site-related features that could play a critical role as damage explanatory factors (Table 2).

These included the distance between each road’s centroid and the coastline ($Distance$), the direction of tsunami wave approach ($WDir$), road orientation ($ROrient$), and a binary factor ($CoastType$) distinguishing between ria and plain coastal typologies characteristic of the Tōhoku region, with a mountainous, indented coastline in the northern part and flat, sandy shoreline in the South of Miyagi and Fukushima prefectures (Mikami et al., 2012; Suppasri et al., 2013, 2015).

Given the significant impact of obstacles and building density on inundation propagation and consequent damage (Rossetto et al., 2007; Reese et al., 2011; Mikami et al., 2012; Rübke & Vött, 2017; Moris et al., 2021; Bernardini et al., 2021; Di Bacco et al., 2023; Zhu et al., 2023), the synthetic variables proposed by Di Bacco et al. (2023) were introduced in this study as proxies to capture potential information on shielding and debris impact mechanisms resulting from the interaction of tsunami

Table 2
Variables in the extended roads MLIT dataset used in this study.

Variable	Description	Data source type
h	Inundation depth at road segment's centroid [m]	Hydrodynamic simulation
v	Flow velocity at road segment's centroid [m s ⁻¹]	Hydrodynamic simulation
Sh	Proxy for shielding effect generated by buildings within the buffer area created at road segment's centroid – buffer in the coastline direction ("coastal buffer") [-]	Geospatial analysis
Sh_R	Proxy for shielding effect generated by buildings within the buffer area created at road segment's centroid – buffer in the inland watercourse direction ("river buffer") [-]	Geospatial analysis
SW	Proxy for shielding effect generated by the presence of seawalls (SW) within the buffer area created at road segment's centroid [-]	Geospatial analysis
DI	Proxy for the debris impact (DI) effect generated by washed-away buildings within the buffer area created at road segment's centroid – buffer in the coastline direction ("coastal buffer") [-]	Geospatial analysis
DI_R	Proxy for the debris impact (DI) effect generated by washed-away buildings within the buffer area created at road segment's centroid – buffer in the inland watercourse direction ("river buffer") [-]	Geospatial analysis
$Distance$	Minimum distance between the road segment's centroid and the coastline [m]	Geospatial analysis
$Distance_R$	Minimum distance between the road segment's centroid and the closest inland watercourse [m]	Geospatial analysis
$WDir$	Probable direction of tsunami wave approach, calculated as the direction of the line of minimum distance between the road segment's centroid and the coastline [°]	Geospatial analysis
$ROrient$	Road orientation, referring to the directional alignment of a road segment, calculated as the rotation angle between the vertices at its two endpoints within a cartesian coordinate system (in this case, EPSG: 2452 – JGD2000) [°]	Geospatial analysis
$CoastType$	Indicator for coast morphology [plain / ria coast]	Surveyed – based on geographical location

propagation with built surfaces. Specifically, following the methodology outlined in Di Bacco et al. (2023), Sh and SW represent the fraction of the area within a buffer region around the road's centroid (as defined below) occupied by buildings and seawalls, respectively:

$$Sh = \frac{\sum_{i=1}^{N_{tot}} A_i}{A_b} \quad \text{and} \quad SW = \frac{\sum_{i=1}^{N_{SW}} L_i h_i}{A_b} \quad (1)$$

where N_{tot} and N_{SW} denote the total number of buildings and seawalls within a buffer area A_b , with A_b , L_i and h_i respectively indicating the footprint area of the i -th building in the buffer, the length and the height of the i -th seawall element. Building information, including reported damage states, was sourced from the corresponding MLIT dataset (2012), while details regarding seawalls were obtained from Di Bacco et al. (2023).

Similarly, to account for the potential impact of collapsed buildings as a source of debris, the variable DI was calculated as a function of only washed-away buildings (N_{wa}) within the buffer area:

$$DI = \frac{\sum_{i=1}^{N_{wa}} A_i}{A_b} \quad (2)$$

The analysis was expanded to include potential effects induced by

inundation caused by the backwater effect of rivers in more inland sections of the affected area (Tanaka et al., 2012; Tanaka & Sato, 2015). To this aim, analogous "river" variables (denoted with a subscript R) were computed in the direction of the nearest inland watercourse: $Distance_R$ represents the distance from each road centroid to the nearest inland watercourse, while Sh_R and DI_R indicate the fractions of the area from each considered road segment to the nearest inland watercourse occupied, respectively, by standing and washed-away buildings.

The coastal and river buffer geometries (Fig. 2) used to calculate the proxy variables were adapted from the approach proposed in Di Bacco et al. (2023) for building damage. The shape of coastal buffers was designed to account for both run-up and backflow mechanisms (Naito et al., 2014; Koïwa et al., 2014; Tachibana, 2015; R bke & V tt, 2017), by combining a frontal coastal buffer and one accounting for the reverse flow (Fig. 2a). In detail, frontal coastal buffers were represented as irregular hexagons, with two sides perpendicular to the line connecting the road centroid and the point of minimum distance to the coastline. The length of each side was assumed to be proportional to $Distance$, except for the side on the centroid, which was limited to a maximum length of 100 m (i.e., the minimum between $Distance/4$ and 100 m). Backflow buffers were only computed when $Distance$ was less than 1000 m, as the backflow effect tends to diminish with increasing distance from the coastline. These buffers were trapezoidal in shape and shared one side with the frontal coastal buffer, using the side adjacent to the centroid as their smaller base. The length of the larger base was set equal to the smaller base plus one-third of the height, calculated based on the centroid-coast distance, as follows: $Distance/4$ if $Distance$ was less than 800 m, $1000 - Distance$ otherwise.

The river buffer (Fig. 2b), oriented towards the nearest inland watercourse, mirrored the design of the frontal coastal buffer, but excluded the geometry for backflow, which is less significant in this direction. Furthermore, the variables Sh_R and DI_R were specifically computed only for road segments where river-induced effects were likely to be relevant, i.e. when $Distance_R$ was less than 500 m and the road was closer to the watercourse than to the coastline ($Distance_R > Distance$).

For visualization purposes, Fig. 1 summarizes the key elements of the extended MLIT dataset, by showing the pairwise relationships and distributions among a subset of features, including hazard (h , v), main velocity proxies (Sh , DI and SW) and distance metrics across the different damage states.

2.2. Model development and feature importance analysis

Extra-Trees (XT) (Geurts et al., 2006) and Random Forest (RF) (Ho, 1995) models were developed for the prediction of the damage state using the variables outlined in the previous section as input. These models were selected due to their demonstrated effectiveness in similar exercises on building damage classification for the same tsunami event (Di Bacco et al., 2023) and for general damage prediction, as in the case of floods (Paulik et al., 2024).

To address the dataset's imbalance arising from the significant proportion of elements in class 0 (no damage), a random resampling strategy was employed to obtain a more even distribution of the data among the four damage states (Fig. 1). Specifically, we sampled and utilized a number of data points from the original elements in class 0 (95,391) that is 25 % greater than the size of the second most represented class in the sample (class 1, with 18,631 elements). After this process, the final dataset for model training comprised 57,454 data points, with 40.5, 32.4, 15.1 and 11.9 % assigned to damage state 0 through 3, respectively. This operation ensures that each class is adequately represented during model training, preventing the model from being skewed towards the majority class; consequently, it promotes a more accurate and robust learning process, enabling the model to generalize effectively and make informed predictions across the entire spectrum of possible outcomes.

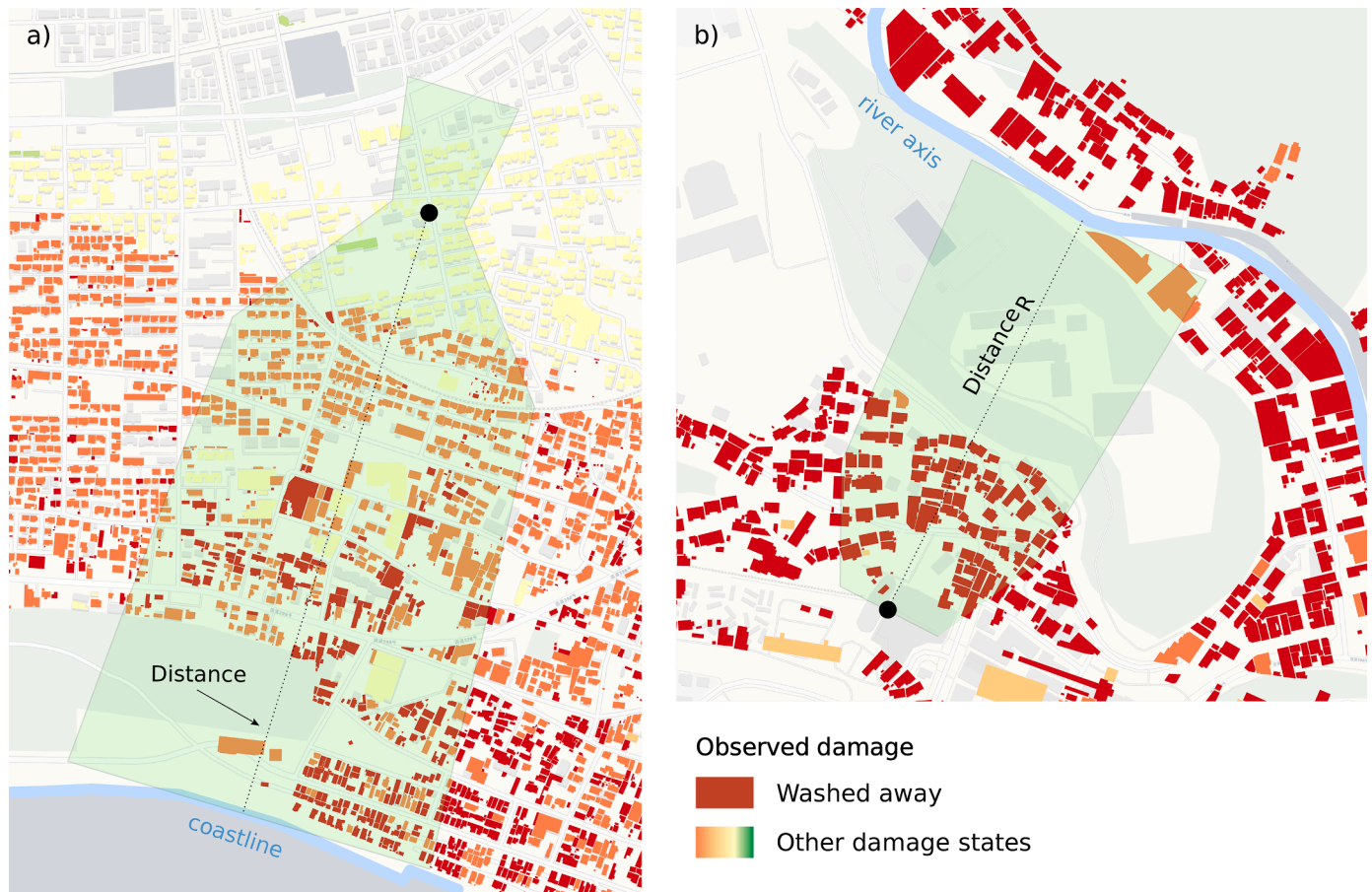


Fig. 2. Calculation of shielding and debris impact proxies: example of buffer geometries for an impacted road. a) Coastal buffer; b) River buffer. $Distance$ and $Distance_R$ denote the minimum distance from the road segment's centroid to either the coastline or the nearest inland watercourse.

The implementation of XT and RF models was carried out in Python, utilizing the scikit-learn library (Pedregosa et al., 2011). Model development was based on the following procedure: a portion (5 %) of the observed data was holdout as a validation set for hyperparameter tuning and the remaining data were then divided into training (95 %) and test (5 %) sets. For each model, an initial random search was conducted to fine-tune models' hyperparameters, which included: the impurity measure criterium, number of estimators, maximum depth of the trees, minimum number of samples per leaf and minimum decrease in impurity for splitting.

The assessment of model accuracy on the test set, averaged over ten training iterations, was based on the relative hit rate (HR), a metric quantifying the proportion of correct predictions to the total number of predictions made. A normalized confusion matrix was also computed for each model to gain deeper insights into the error patterns.

A comparative analysis was conducted to evaluate the performances of various models trained using different combinations of input features. These combinations varied in terms of data type, enabling an investigation into the sensitivity of model accuracy to the comprehensiveness and complexity (in terms of retrieval and/or pre-processing costs) of the input data considered for model development. In detail, the reference Run 1 served as the initial benchmark, encompassing the minimum set of variables retained across all subsequent models. This baseline incorporated only inundation depth information (h) and coast-related geospatial features requiring a straightforward calculation ($Distance$, $WDir$, and $ROrient$) or imputation ($CoastType$). Starting from this reference run, additional model configurations were generated to account for further potential explanatory aspects of the damage mechanisms. First, hydrodynamic information was included, either directly through flow velocity

(v , Run 2) or indirectly via the two proxy variables Sh and DI (Run 3). Then, the following two models incorporated into the baseline the features describing the potential contribution of the river network to the inundation, starting with only $Distance_R$ in Run 4 and then including also the shielding and debris effects in the direction of the nearest watercourse (Sh_R and DI_R , Run 5). Finally, Run 6 integrated the drivers identified as strong predictors in the previous model configurations, with a preference, in case of features providing equivalent information (such as velocity and its proxies), to those characterized by a less demanding computation for their assessment. In this analysis, the consideration of road type information was omitted due to the limited number of elements associated with this attribute in the dataset.

The relative mean decrease in accuracy (mda) was employed to assess the importance of the individual features within the models. This involved systematically shuffling each feature in ten iterations and quantifying the resulting change in accuracy compared to the original one.

2.3. Insights from explainable machine learning: converting model outcomes into fragility functions

The analysis proceeded with an additional phase, aimed at providing a physical interpretation of the cause-effect relationships in tsunami damage on roads while also addressing a common critique of machine learning as a "black-box" approach (Marcinkevičs & Vogt, 2023). This was achieved by transforming model outcomes into visually interpretable plots, resembling the classical fragility functions, with associated uncertainty bands to reflect the multi-variable nature of tsunami damage.

In this phase, the most complete and performing model was selected to represent the output across key informative features, hereinafter referred to as “Investigated Feature” (IF). These included topographical and geographical factors, such as *CoastType*, *Distance*, *Distance_R*, as well as direct (*v*) or indirect (*Sh* and *SW*) velocity-related features of the event.

To visualize the fragility functions, the trained model was applied to sampled data points from the extended MLIT dataset, which ensures a robust representation without assuming any correlation among the input features. For illustrative purposes, the fragility functions were generated using fixed values of the IF. For *CoastType*, both possible classes were considered, while for continuous features, these values were selected based on the lower, median and upper quartiles of the IF in the dataset.

Consistently with conventional practices in tsunami literature (Koshimura et al., 2009; Charvet et al., 2017; Williams et al., 2020), inundation depth was selected as the primary intensity measure for constructing the fragility functions. Percentiles of inundation depth (*h*) were computed at 5 % intervals, resulting in 21 distinct values, including minimum and maximum *h* values, totaling 20 values by averaging interval extremes. For each *h* interval, 200 road segments were sampled with replacement, and desired values for the IF (e.g., *CoastType* = “Ria” / “Plain”, or fixed values for continuous variables) were assigned. This process generated a dataset comprising 200 data · 20 intervals · *n* values for investigation. Subsequently, for each (*h*, IF) pair, 200 damage state predictions were produced. The probabilities of reaching each damage state were then calculated by determining the relative number of times a specific damage state was reached or exceeded across the 200 predictions. This procedure was iterated 200 times for each (*h*, IF) combination to ensure a stability of the generated fragility functions. Finally, for each (*h*, IF) pairing, values representing the 10th percentile, median, and 90th percentile were computed and integrated into monotonically increasing functions and confidence

intervals to provide an informative representation of predictive uncertainty. The number of samples and iterations for deriving the fragility functions and associated bands was determined in a preliminary phase aimed at ensuring result stability while keeping feasible computational times.

3. Results and discussion

3.1. Model performance and analysis of feature importance

Fig. 3 provides a comprehensive overview of the results, summarizing the feature importance and relative hit rate (HR) for XT and RF models trained with six different input configurations (Run 1 to 6), as described in Section 2.2. The radial plots report the mean decrease in accuracy (mda) associated with each feature across the different models. Each wedge’s radius represents the degree to which the model’s accuracy decreases when a specific feature is randomly shuffled during model training. Features with higher mda values are considered more crucial for the model’s performance. The color scheme in the plot distinguishes between the RF and XT models, with the overlapping area appearing in green as a result of using a transparent yellow fill and dashed border for RF and transparent cyan fill and solid border for XT. Gray shading indicates the variables that are not included in the different model configurations.

In addition to the overall results, Fig. 4 presents the confusion matrices for Runs 1 and 6. These matrices, describing hit and misclassification rates among the different damage states, indicate that damage states 0, 1, and 3 are more easily identified, whereas class 2 exhibits higher misclassification rates, as typical in central damage classes subject to larger identification uncertainties in post-event field surveys (Endo et al., 2018; Lin et al., 2018). The results in Figs. 3 and 4 reveal highly comparable performance between XT and RF, maintaining a consistent hierarchy of feature importance across models’

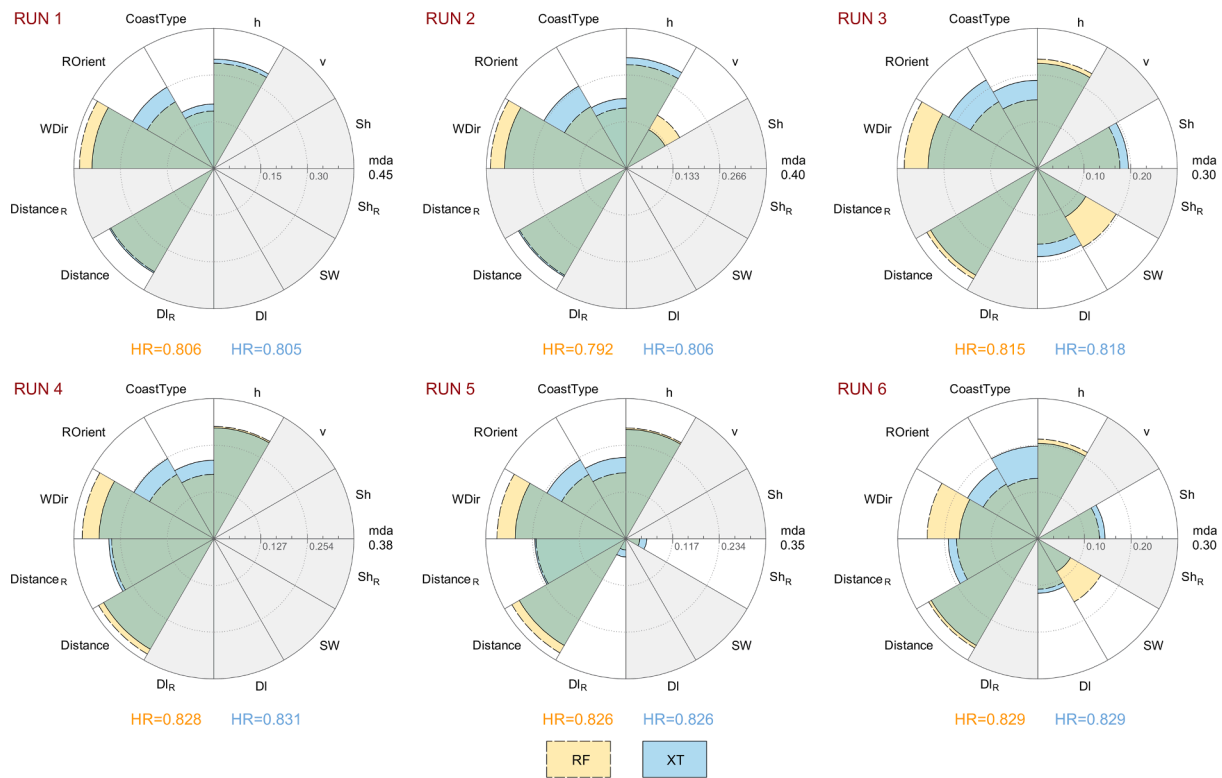


Fig. 3. Results of the feature importance analysis and global accuracy (HR) for RF (transparent yellow fill) and XT (transparent cyan fill) models trained with different combinations of input variables (Run 1–6). Overlap region between the two models appears in green. Gray shading indicates the features that are not included in each model configuration.

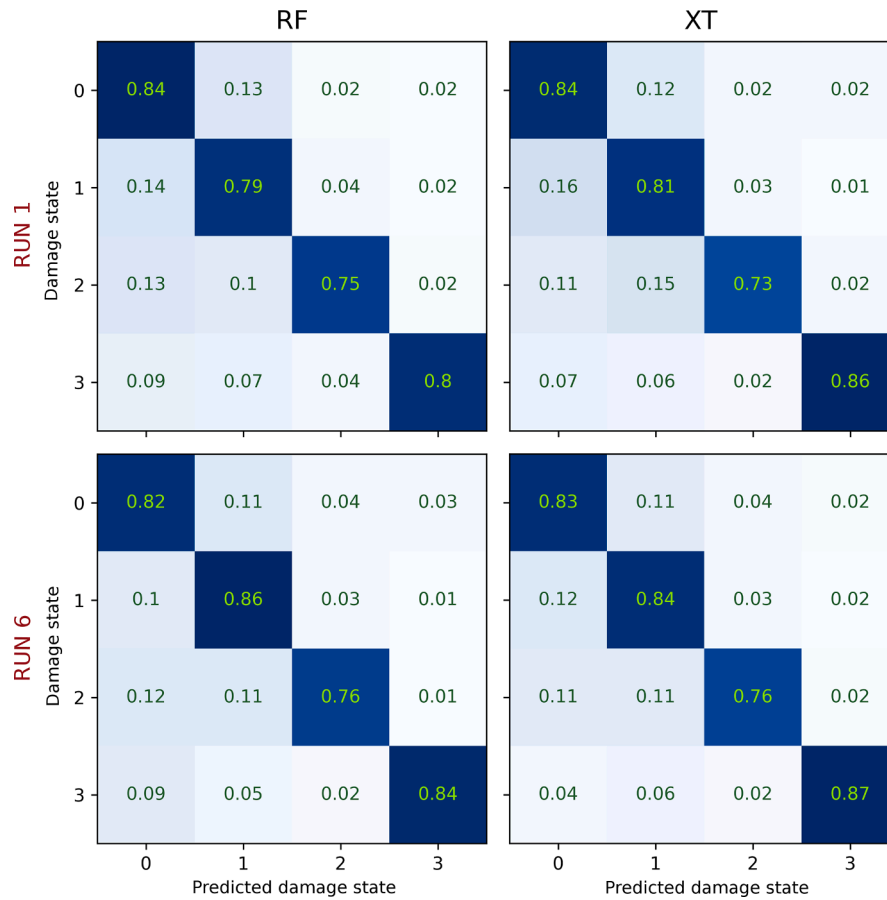


Fig. 4. Normalized confusion matrices for run 1 and 6 (input variables as in Fig. 3) for RF (left) and XT (right) models.

configurations. The major differences between the two models stems instead from the random nature of the splitting procedure in XT, which tends to favor categorical or categorical-like features, such as *CoastType* and *ROrient*, with the latter, albeit continuous, exhibiting data clustering at multiples of 90° and then effectively resembling a distribution with four distinct classes (Fig. 5, left panel).

Overall accuracy ranges between 0.79 and 0.83, aligning with analogous models developed for buildings for the same tsunami event (Di Bacco et al., 2023).

Based on the relative mean decrease in accuracy (Fig. 3), inundation depth (*h*) and its closely related variable, the distance from the coastline (*Distance*), emerge as important predictors, being them descriptive of the

tsunami intensity (Rossetto et al., 2007; Röbbke & Vött, 2017). This confirms the well-known critical need for detailed information on inundation scenarios for both ex-ante and ex-post damage assessments (Scorzini et al., 2022). Other variables hold nearly comparable importance in predicting damage to roads, in a more pronounced manner than observed in similar tests conducted in the case of buildings (Di Bacco et al., 2023; Scorzini et al., 2024). Indeed, the models consistently highlight the importance of the wave approach angle relative to the coast (*WDir*) and road orientation angle (*ROrient*), with their combined effect providing meaningful information on the road’s orientation in relation to tsunami’s direction. Specifically, the continuous variable *WDir* (Fig. 5, right panel) stands out as one of the most influential features, while *ROrient* (Fig. 5, left panel), especially in the case of RF, retains strong but slightly lesser importance, comparable to that observed for *Distance_R*. These quantitative findings align with narratives from previous studies on tsunami events. For instance, Ratnasooriya et al. (2007) documented severe damage for roads parallel to the coastline compared to those running perpendicular to it for the 2004 Indian Ocean tsunami in Sri Lanka, while Tanaka et al. (2012) and Tanaka and Sato (2015) described river-induced inundation mechanisms observed for the Tōhoku tsunami.

Unlike damage models for buildings, where shielding and debris effects are considered crucial (Reese et al., 2011; Di Bacco et al., 2023; Scorzini et al., 2024), the impact of such factors on roads appears to be more limited, although still not negligible (Fig. 3). The minor importance of such factors, which can be seen as proxies for local hydrodynamic factors of tsunami propagation on land (Scorzini et al., 2024), is further confirmed by the comparable lower importance of direct velocity information from the detailed numerical simulation of the event (*v*). In this context, a more significant role is observed for the shielding effect induced by buildings (*Sh*) and seawalls (*SW*), with the second described

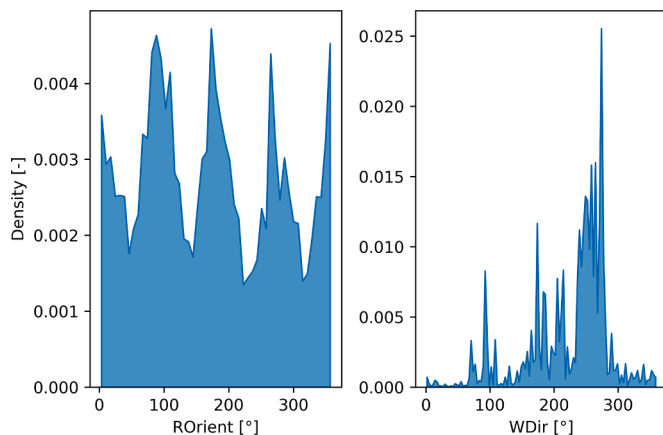


Fig. 5. Density plots for road orientation (*ROrient*) and the probable direction of tsunami wave approach (*WDir*) in the extended MLIT dataset.

in other studies to have a controversial effect on tsunami damage, i.e. with a positive mitigating impact in some cases and null or negligible in others (Rossetto et al., 2007; Mimura et al., 2011; Mikami et al., 2012).

Furthermore, it can be observed that as the number of predictors increases, the accuracy does not undergo substantial improvements (Fig. 3). The minimal set of features necessary to achieve an HR of approximately 0.8 includes only the inundation depth and other geospatial variables that can be efficiently derived even at large scale (and ex-ante) through simple geoprocessing operations and not requiring extensive data collection efforts.

In detail, the inclusion of velocity (Run 2) to the baseline model (Run 1, with HR ~ 0.80) does not result in an overall performance improvement (Fig. 3), as the information brought by v is intrinsically contained in h , given that they are theoretically related through the shallow water equations ($v \sim \sqrt{gh}$), as also visible in Fig. 1. However, the introduction of velocity-related proxies (Sh , DI , and SW - Run 3), characterized by a negligible correlation with h (Fig. 1), raises the HR to 0.82, highlighting the significance, although to a modest extent, of hydrodynamic aspects for road damage estimation. In Run 4, mirroring Run 1 with the addition of $Distance_R$, a noticeable increase in accuracy is observed (HR ~ 0.83), suggesting the potential contribution of local flooding from inland watercourses, as described in Tanaka et al. (2012)

and Tanaka and Sato (2015). On the other hand, the incorporation of shielding and debris impact information in the direction of inland watercourses (Run 5) does not improve the performance compared to the previous run. This indicates that such effects in secondary directions are less influential and, therefore, negligible for tsunami damage modeling. The combined effect of all variables, identified incrementally as good predictors, is represented in Run 6, which maintains a consistent accuracy of about 0.83, thus emphasizing their suitability in describing tsunami damage mechanisms to roads.

Overall, an interesting result is that no single variable distinctly stands out as key explicative feature for road damage. This confirms that relying on univariate models, as often seen in the literature through fragility functions expressing damage based solely on inundation depth, may offer substantial limitations, even in a more critical way than occurring for buildings (Di Bacco et al., 2023; Vescovo et al., 2023; Scorzini et al., 2024).

3.2. Insights from explainable machine learning: converting model outcomes into fragility functions

Building upon the insights gained from the feature importance analysis, the focus now shifts to emphasizing the complex, multi-

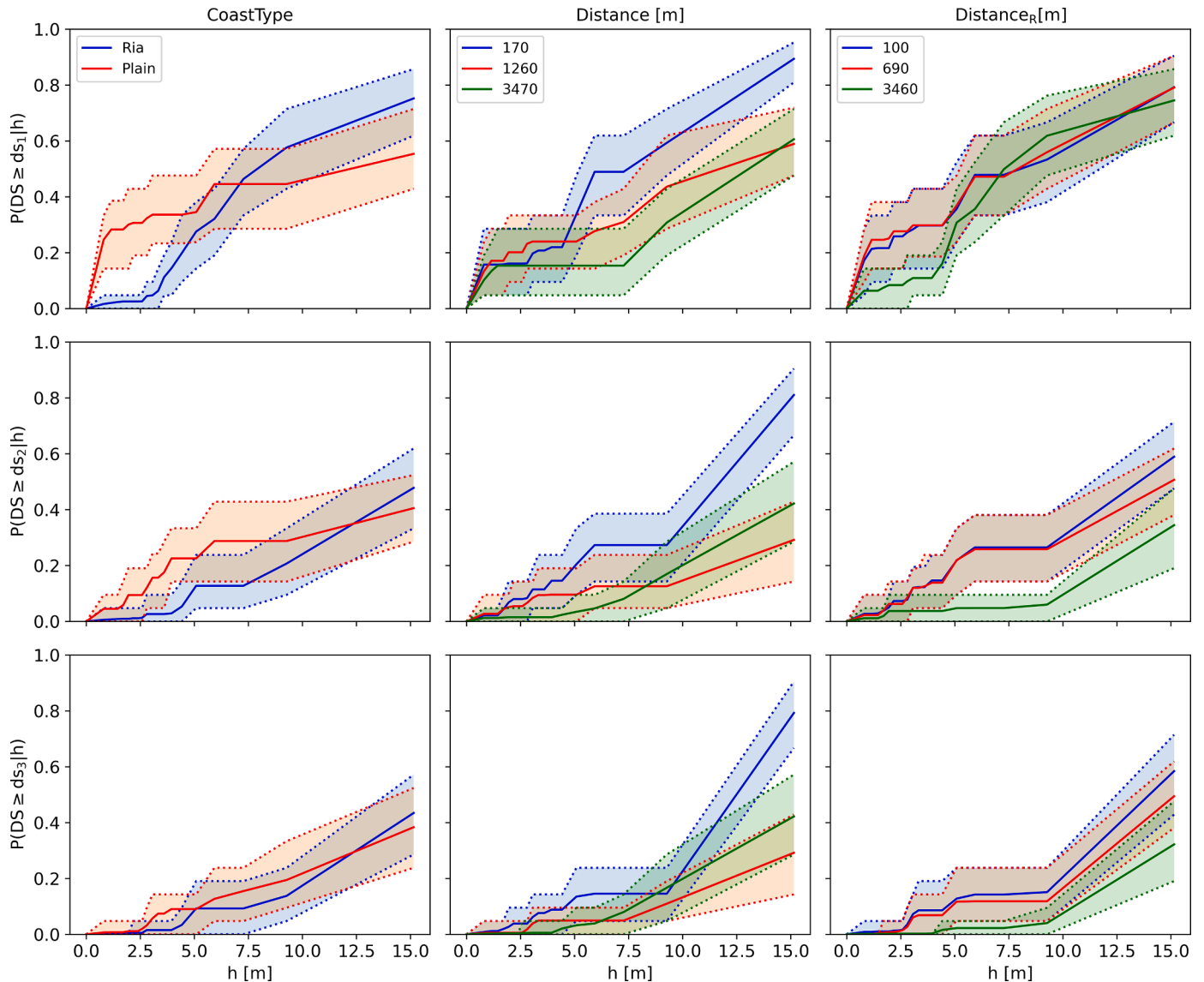


Fig. 6. XT-derived fragility functions with 10th-90th confidence intervals for fixed values of $CoastType$, $Distance$ and $Distance_R$.

variable relationships influencing damage mechanisms, thereby highlighting the limitations of standard univariate approaches in damage modeling. To illustrate this, outcomes from the most complete XT-based Run 6 were utilized to construct traditional fragility functions. These functions were generated here for fixed values of the investigated feature and included, in addition to the central values, 10th - 90th confidence intervals to provide a comprehensive understanding of the associated predictive uncertainty.

As examples, Figs. 6 and 7 show the resulting fragility functions for the “minor” (ds_1), “moderate” (ds_2), and “severe” (ds_3) damage states, considering fixed values of geographical and velocity-related features. For the latter, to isolate the individual contribution to the fragility functions of the three homologous variables (v and its proxies, Sh and SW), the configuration of Run 6 was adapted by excluding each of them in turn from model development.

The fragility functions derived for the two coastal settings in the study area reveal interesting patterns (Fig. 6, left panel). Roads in “plain” coasts exhibit higher vulnerability, especially for shallower water depths (up to 5 m), diverging from findings in previous studies on building damage, where “ria” coasts have been described to be subject to amplifying damage mechanisms due to their specific morphological features (Suppasri et al., 2013, 2015; De Risi et al., 2017). This greater

vulnerability of roads in plain coastal settings may stem from the substantial importance of road’s geometric layout in relation to the direction of wave approach, as revealed from the results of the feature importance analysis as well as from empirical observations in other events (Ratnasooriya et al., 2007). This highlights that geometric factors can play a more crucial role in predictive accuracy than hydrodynamic variables. However, an inversion of this trend emerges for higher water depths (>6 m), mirroring a similar pattern observed in the literature for building damage, but in the opposite direction (Suppasri et al., 2013, 2015). This suggests that the influence of geometric factors related to road layout diminishes when the event’s intensity is particularly high, with hydraulic aspects becoming more influential on the damage mechanism. For the most severe damage states, although distinct trends for the median functions can be detected for the two coastal typologies, the broad and overlapping uncertainty bands in Fig. 6 indicate that reaching a certain damage state results from a combination of several factors, challenging the use of univariate fragility functions for reliable damage assessment.

Distance from the coast emerged as a key factor influencing predictive accuracy (Fig. 3) and this is further evident in the corresponding fragility functions obtained for *Distance* values of 170, 1260, and 3470 m (Fig. 6, central panel). A negative correlation exists between *Distance*

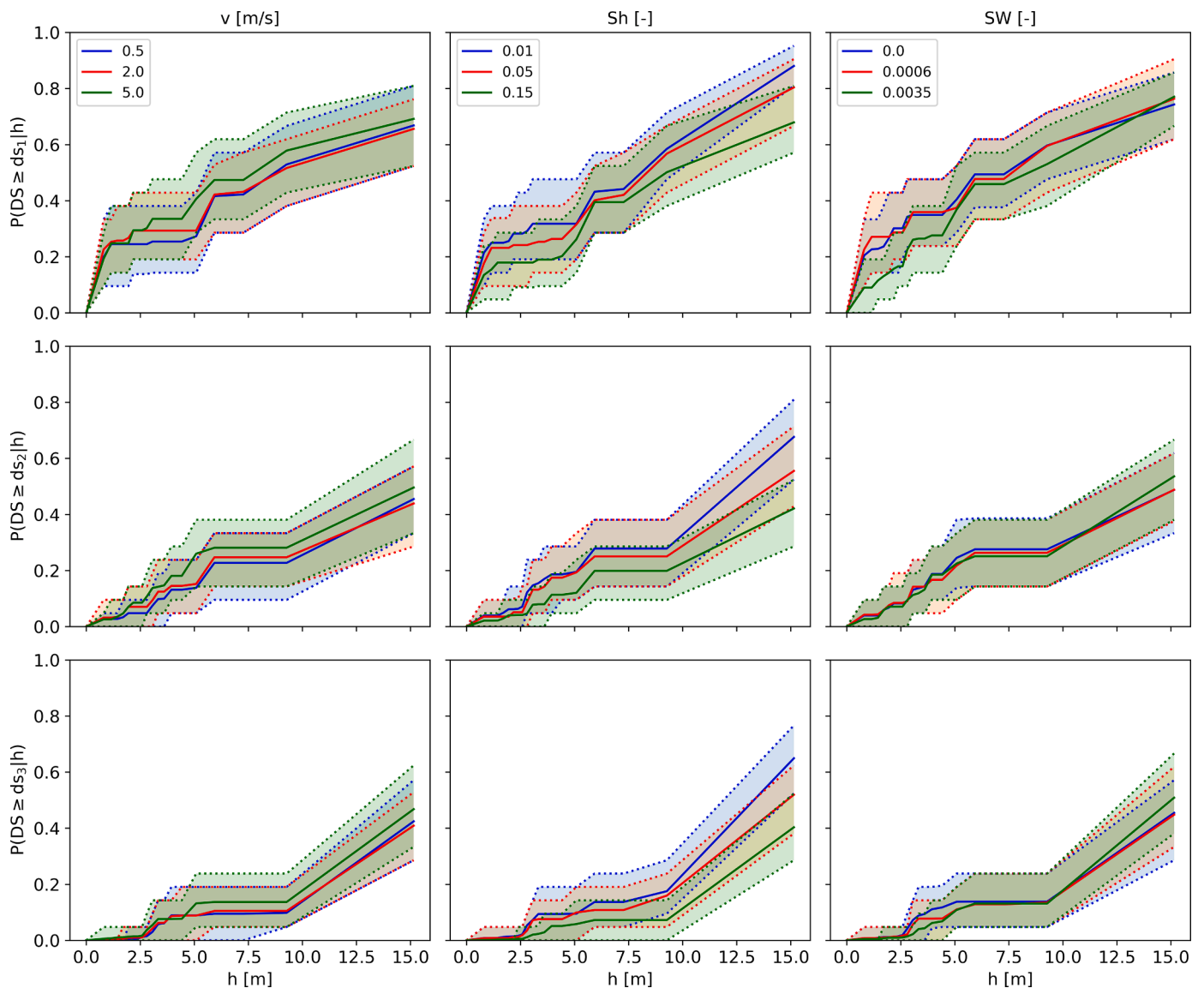


Fig. 7. XT-derived fragility functions with 10th-90th confidence intervals for fixed values of velocity-related variables: v , Sh and SW .

and inundation depth, with roads closer to the coast being more susceptible to damage (Figs. 1 and 6). More pronounced differences in the fragility patterns are observed for less severe damage states; conversely, in ds_3 , the resulting functions for roads beyond 1 km from the coastline are nearly overlapping, while a substantial increase in the probability of reaching this state is observed only in close proximity to the coast. Similarly, the possible influence of inundation caused by the backflow of watercourses is also evident in Fig. 6 (right panel), with roads closer to them exhibiting higher susceptibility, particularly for $Distance_R$ below 700 m. This effect significantly diminishes (especially for ds_2 and ds_3) with increasing $Distance_R$, except for ds_1 , where a different trend is observed for $h > 6$ m, although probably influenced by specific local factors.

The mitigation effect exerted by the presence of built-up areas and seawalls is evident in the fragility functions represented in the central and right panels of Fig. 7, where a reduced probability of reaching a specific damage state can be observed with increasing values of Sh and SW (i.e., with a higher incidence of buildings and seawalls within the buffer areas at roads' centroids). The differences are less marked for SW , especially for ds_2 and ds_3 , while in ds_1 the protective effect of seawalls appears to become negligible in case of high inundation depths ($h > 5$ m), in line with qualitative observations reported in Mimura et al. (2011) and Mikami et al. (2012). Only slight differences are also visible in the median fragility functions derived for different velocity values (Fig. 7, left panel), with considerable overlap across all damage states, as well as within all associated uncertainty bands, especially for $v \leq 2$ m s^{-1} .

However, the most interesting result from Figs. 6 and 7 is that, in all cases, despite the general trends, the impact of other features tends to blur the distinctions among the central values of the fragility functions.

This reaffirms the findings from the feature importance analysis, emphasizing that there is no dominant variable governing the damage mechanisms for roads, rendering the expression of a model based solely on inundation depth less meaningful. This observation underscores the critical need to move beyond traditional univariate fragility functions in favor of multi-variable models, which are inherently capable of accounting for the complex interactions among key features influencing the damage process.

4. Conclusions

The present study aimed to enhance understanding of road damage mechanisms during tsunami events, utilizing a machine learning approach on an extended version of the dataset compiled by the Japanese Ministry of Land, Infrastructure, Transport and Tourism (MLIT) in the aftermath of the 2011 Great East Japan tsunami.

The developed models provided insights into the multi-variable nature of tsunami-induced damage to roads, highlighting the inadequacy of traditional fragility functions and the potential of multi-variable vulnerability models for refining tsunami impact assessments. Differently from buildings, where inundation depth typically dominates as the key feature, road damage exhibits a more intricate interplay of variables. Although inundation depth remains a crucial factor, the analysis presented in this study emphasized the significance of other features, including the wave approach angle, the road orientation angle and the indicator accounting for the presence of seawalls. While information on hydrodynamic features associated with tsunami inundation modestly influenced overall performance, the distance from inland watercourses also demonstrated a noticeable contribution.

These insights can provide modelers and stakeholders with valuable information to optimize resource allocation for damage modeling in both ex-ante risk assessment phases and post-event emergency response, facilitating more efficient and informed decisions. In this context, the straightforward computation of most identified key features, which can be derived using simple geospatial operations, brings significant added value to the efficiency of the modeling process. Furthermore, the proposed modeling framework has also significant potential for replication

in diverse geographical regions. As new datasets become available, machine learning approaches hold promise for widespread applicability, making them versatile tools for disaster risk assessment across various contexts. Improved model outcomes, coupled with explicit treatment of modeling uncertainties and efficient input data retrieval, can then contribute to enhanced effectiveness of risk management processes.

CRedit authorship contribution statement

Mario Di Bacco: Writing – review & editing, Visualization, Methodology, Investigation, Formal analysis, Data curation, Conceptualization. **James H. Williams:** Writing – review & editing, Data curation. **Daisuke Sugawara:** Writing – review & editing, Data curation. **Anna Rita Scorzini:** Writing – original draft, Visualization, Resources, Methodology, Investigation, Data curation, Conceptualization.

Declaration of competing interest

The authors declare that they have no known competing financial interests or personal relationships that could have appeared to influence the work reported in this paper.

Data availability

Data will be made available on request.

References

- Ballantyne, D. (2006). Sri Lanka lifelines after the December 2004 Great Sumatra earthquake and tsunami. *Earthquake Spectra*, 22, 545–559. <https://doi.org/10.1193/1.2211367>
- Bernardini, G., Romano, G., Soldini, L., & Quagliarini, E. (2021). How urban layout and pedestrian evacuation behaviours can influence flood risk assessment in riverine historic built environments. *Sustainable Cities and Society*, 70, Article 102876. <https://doi.org/10.1016/j.scs.2021.102876>
- Charvet, I., Macabuag, J., & Rossetto, T. (2017). Estimating tsunami-induced building damage through fragility functions: Critical review and research needs. *Frontiers in Built Environment*, (1–22), 36. <https://doi.org/10.3389/fbuil.2017.00036>
- Chen, J., Huang, Z., Jiang, C., Deng, B., & Long, Y. (2013). Tsunami-induced scour at coastal roadways: A laboratory study. *Natural Hazards*, 69, 655–674. <https://doi.org/10.1007/s11069-013-0727-6>
- Davis, S., Clopper, P., Parola, A., Males, R., & Rogers, C. (2013). Development of a model of flood damage to roads. In C. L. Patterson, S. D. Struck, & D. J. Murray (Eds.), *World Environmental and Water Resources Congress 2013: Showcasing the Future* (pp. 2382–2390). <https://doi.org/10.1061/9780784412947.234>
- De Risi, R., Goda, K., Yasuda, T., & Mori, N. (2017). Is flow velocity important in tsunami empirical fragility modeling? *Earth-Science Reviews*, 166, 64–82. <https://doi.org/10.1016/j.earscirev.2016.12.015>
- Di Bacco, M., Rotello, P., Suppasri, A., & Scorzini, A. R. (2023). Leveraging data driven approaches for enhanced tsunami damage modelling: Insights from the 2011 Great East Japan event. *Environmental Modelling & Software*, 160, Article 105604. <https://doi.org/10.1016/j.envsoft.2022.105604>
- Edwards, C. (2006). Thailand lifelines after the December 2004 Great Sumatra earthquake and Indian Ocean tsunami. *Earthquake Spectra*, 22, 641–659. <https://doi.org/10.1193/1.2204931>
- Endo, Y., Adriano, B., Mas, E., & Koshimura, S. (2018). New insights into multiclass damage classification of tsunami-induced building damage from SAR images. *Remote Sensing*, 10(12), 2059. <https://doi.org/10.3390/rs10122059>
- Fritz, H. M., Petroff, C. M., Catalán, P. A., Cienfuegos, R., Winckler, P., Kalligeris, N., ... Synolakis, C. E. (2011). Field survey of the 27 February 2010 Chile tsunami. *Pure and Applied Geophysics*, 168, 1989–2010. <https://doi.org/10.1007/s00024-011-0283-5>
- Geurts, P., Ernst, D., & Wehenkel, L. (2006). Extremely randomized trees. *Machine Learning*, 63, 3–42. <https://doi.org/10.1007/s10994-006-6226-1>
- Haque, S., Ikeuchi, K., Shrestha, B. B., Kawasaki, A., & Minamide, M. (2023). Establishment of flood damage function model for rural roads: A case study in the Teesta River basin, Bangladesh. *Progress in Disaster Science*, 17, Article 100269. <https://doi.org/10.1016/j.pdisas.2022.100269>
- Ho, T. K. (1995). Random decision forests. In , 1. *Proceedings of the 3rd International Conference on Document Analysis and Recognition* (pp. 278–282). <https://doi.org/10.1109/ICDAR.1995.598994>
- Kazama, M., & Noda, T. (2012). Damage statistics (Summary of the 2011 off the Pacific Coast of Tohoku Earthquake damage). *Soils and Foundations*, 52(5), 780–792. <https://doi.org/10.1016/j.sandf.2012.11.003>
- Koiwa, N., Kasai, M., Kataoka, S., & Isono, T. (2014). Examination of relation with tsunami behavior reconstructed from on-site sequence photographs, topography, and sedimentary deposits from the 2011 Tohoku-oki tsunami on the Kamikita Plain,

- Japan. *Marine Geology*, 358, 107–119. <https://doi.org/10.1016/j.margeo.2014.08.009>
- Koshimura, S., Namegaya, Y., & Yanagisawa, H. (2009). Tsunami fragility: A new measure to identify tsunami damage. *Journal of Disaster Research*, 4(6), 479–488. <https://doi.org/10.20965/jdr.2009.p0479>
- Kreibich, H., Piroth, K., Seifert, I., Maiwald, H., Kunert, U., Schwarz, J., Merz, B., & Thieken, A. H. (2009). Is flow velocity a significant parameter in flood damage modelling? *Natural Hazards and Earth System Sciences*, 9(5), 1679–1692. <https://doi.org/10.5194/nhess-9-1679-2009>
- Lin, S. L., Uma, S. R., & King, A. (2018). Empirical fragility curves for non-residential buildings from the 2010–2011 Canterbury earthquake sequence. *Journal of Earthquake Engineering*, 22(5), 749–777. <https://doi.org/10.1080/13632469.2016.1264322>
- Macabuag, J., Rossetto, T., Ioannou, I., Suppasri, A., Sugawara, D., Adriano, B., Imamura, F., Eames, I., & Koshimura, S. (2016). A proposed methodology for deriving tsunami fragility functions for buildings using optimum intensity measures. *Natural Hazards*, 84, 1257–1285. <https://doi.org/10.1007/s11069-016-2485-8>
- Mallick, R. B., Tao, M., Daniel, J. S., Jacobs, J., & Veeraragavan, A. (2017). Development of a methodology and a tool for the assessment of vulnerability of roadways to flood-induced damage. *Journal of Flood Risk Management*, 10(3), 301–313. <https://doi.org/10.1111/jfr3.12135>
- Marcinkevics, R., & Vogt, J. E. (2023). Interpretable and explainable machine learning: A methods-centric overview with concrete examples. *Wiley Interdisciplinary Reviews: Data Mining and Knowledge Discovery*, 13, e1493. <https://doi.org/10.1002/widm.1493>
- Marín-García, D., Rubio-Gómez-Torga, J., Duarte-Pinheiro, M., & Moyano, J. (2023). Simplified automatic prediction of the level of damage to similar buildings affected by river flood in a specific area. *Sustainable Cities and Society*, 88, Article 104251. <https://doi.org/10.1016/j.scs.2022.104251>
- Maruyama, Y., & Itagaki, O. (2017). Development of tsunami fragility functions for ground-level roads. *Journal of Disaster Research*, 12(1), 131–136. <https://doi.org/10.20965/jdr.2017.p0131>
- Mikami, T., Shibayama, T., Esteban, M., & Matsumaru, R. (2012). Field survey of the 2011 Tohoku earthquake and tsunami in Miyagi and Fukushima prefectures. *Coastal Engineering Journal*, 54(1), Article 1250011. <https://doi.org/10.1142/S0578563412500118>
- Mimura, N., Yasuhara, K., Kawagoe, S., Yokoki, H., & Kazama, S. (2011). Damage from the Great East Japan Earthquake and Tsunami—a quick report. *Mitigation and Adaptation Strategies for Global Change*, 16, 803–818. <https://doi.org/10.1007/s11027-011-9297-7>
- Moris, J. P., Kennedy, A. B., & Westerink, J. J. (2021). Tsunami wave run-up load reduction inside a building array. *Coastal Engineering*, 169, Article 103910. <https://doi.org/10.1016/j.coastaleng.2021.103910>
- Naito, C., Cercone, C., Riggs, H. R., & Cox, D. (2014). Procedure for site assessment of the potential for tsunami debris impact. *Journal of Waterway, Port, Coastal, and Ocean Engineering*, 140(2), 223–232. [https://doi.org/10.1061/\(ASCE\)JWW.1943-5460.0000222](https://doi.org/10.1061/(ASCE)JWW.1943-5460.0000222)
- Paulik, R., Wild, A., Zorn, C., Wotherspoon, L., & Williams, S. (2024). Evaluation of residential building damage for the July 2021 flood in Westport, New Zealand. *Geoscience Letters*, 11(1), 15. <https://doi.org/10.1186/s40562-024-00323-z>
- Paulik, R., Williams, J. H., Horspool, N., Catalan, P. A., Mowll, R., Cortés, P., & Woods, R. (2021). The 16 September 2015 Illapel earthquake and tsunami: Post-event tsunami inundation, building and infrastructure damage survey in Coquimbo, Chile. *Pure and Applied Geophysics*, 178(12), 4837–4851. <https://doi.org/10.1007/s00024-021-02734-x>
- Pedregosa, F., Varoquaux, G., Gramfort, A., Michel, V., Thirion, B., Grisel, O., ... Duchesnay, É. (2011). Scikit-learn: Machine learning in Python. *Journal of Machine Learning Research*, 12, 2825–2830.
- Ratnasooriya, H. A., Samarawickrama, S. P., & Imamura, F. (2007). Post tsunami recovery process in Sri Lanka. *Journal of Natural Disaster Science*, 29(1), 21–28. <https://doi.org/10.2328/jnds.29.21>
- Rebally, A., Valeo, C., He, J., & Saidi, S. (2021). Flood impact assessments on transportation networks: A review of methods and associated temporal and spatial scales. *Frontiers in Sustainable Cities*, 3, Article 732181. <https://doi.org/10.3389/frsc.2021.732181>
- Reese, S., Bradley, B. A., Bind, J., Smart, G., Power, W., & Sturman, J. (2011). Empirical building fragilities from observed damage in the 2009 South Pacific tsunami. *Earth-Science Reviews*, 107(1–2), 156–173. <https://doi.org/10.1016/j.earscirev.2011.01.009>
- Röbke, B. R., & Vött, A. (2017). The tsunami phenomenon. *Progress in Oceanography*, 159, 296–322. <https://doi.org/10.1016/j.pocan.2017.09.003>
- Rossetto, T., Peiris, N., Pomonis, A., Wilkinson, S. M., Del Re, D., Koo, R., & Gallocher, S. (2007). The Indian Ocean tsunami of december 26, 2004: Observations in Sri Lanka and Thailand. *Natural Hazards*, 42, 105–124. <https://doi.org/10.1007/s11069-006-9064-3>
- Samela, C., Carisi, F., Domeneghetti, A., Petrucci, N., Castellari, A., Iacobini, F., Rinaldi, A., Zammuto, A., & Brath, A. (2023). A methodological framework for flood hazard assessment for land transport infrastructures. *International Journal of Disaster Risk Reduction*, 85, Article 103491. <https://doi.org/10.1016/j.ijdrr.2022.103491>
- Scorzini, A. R., Dewals, B., Rodriguez Castro, D., Archambeau, P., & Molinari, D. (2022). INSYDE-BE: Adaptation of the INSYDE model to the Walloon region (Belgium). *Natural Hazards and Earth System Sciences*, 22(5), 1743–1761. <https://doi.org/10.5194/nhess-22-1743-2022>
- Scorzini, A. R., Di Bacco, M., Sugawara, D., & Suppasri, A. (2024). Machine learning and hydrodynamic proxies for enhanced rapid tsunami vulnerability assessment. *Communications Earth & Environment*, 5(1), 301. <https://doi.org/10.1038/s43247-024-01468-7>
- Sugawara, D. (2018). Evolution of numerical modeling as a tool for predicting tsunami-induced morphological changes in coastal areas: A review since the 2011 Tohoku Earthquake. In V. Santiago-Pandino, S. Sato, N. Maki, & K. Iuchi (Eds.), *The 2011 Japan earthquake and tsunami: Reconstruction and restoration. Insights and assessment after 5 years. Advances in natural and technological hazards research* (pp. 451–467). Cham, Switzerland: Springer.
- Sugawara, D., & Goto, K. (2012). Numerical modeling of the 2011 Tohoku-oki tsunami in the offshore and onshore of Sendai Plain, Japan. *Sedimentary Geology*, 282, 110–123. <https://doi.org/10.1016/j.sedgeo.2012.08.002>
- Sugawara, D., Takahashi, T., & Imamura, F. (2014). Sediment transport due to the 2011 Tohoku-oki tsunami at Sendai: Results from numerical modeling. *Marine Geology*, 358, 18–37. <https://doi.org/10.1016/j.margeo.2014.05.005>
- Suppasri, A., Charvet, I., Imai, K., & Imamura, F. (2015). Fragility curves based on data from the 2011 Tohoku-oki tsunami in Ishinomaki city, with discussion of parameters influencing building damage. *Earthquake Spectra*, 31(2), 841–868. <https://doi.org/10.1193/053013EQS138M>
- Suppasri, A., Mas, E., Charvet, I., Gunasekera, R., Imai, K., Fukutani, Y., Abe, Y., & Imamura, F. (2013). Building damage characteristics based on surveyed data and fragility curves of the 2011 Great East Japan tsunami. *Natural Hazards*, 66, 319–341. <https://doi.org/10.1007/s11069-012-0487-8>
- Tang, A., Ames, D., McLaughlin, J., Murugesu, G., Plant, G., Yashinsky, M., ... Gandhi, P. (2006). Coastal Indian lifelines after the 2004 Great Sumatra earthquake and Indian Ocean tsunami. *Earthquake spectra*, 22(3 suppl), 607–639. <https://doi.org/10.1193/1.2206089>
- Tachibana, T. (2015). Inundation behavior of the 2011 Tohoku earthquake tsunami in the Taro District, Miyako City, northeast Japan, as inferred from directional traces. *Natural Hazards*, 75(3), 2311–2330. <https://doi.org/10.1007/s11069-014-1427-6>
- Tanaka, N., & Sato, M. (2015). Scoured depth and length of pools and ditches generated by overtopping flow from embankments during the 2011 Great East Japan Tsunami. *Ocean Engineering*, 109, 72–82. <https://doi.org/10.1016/j.oceaneng.2015.08.053>
- Tanaka, N., Yagisawa, J., & Yasuda, S. (2012). Characteristics of damage due to tsunami propagation in river channels and overflow of their embankments in Great East Japan Earthquake. *International Journal of River Basin Management*, 10(3), 269–279. <https://doi.org/10.1080/15715124.2012.694365>
- Tarbotton, C., Dall'Osso, F., Dominey-Howes, D., & Goff, J. (2015). The use of empirical vulnerability functions to assess the response of buildings to tsunami impact: Comparative review and summary of best practice. *Earth-Science Reviews*, 142, 120–134. <https://doi.org/10.1016/j.earscirev.2015.01.002>
- Unjoh, S. (2012). Tsunami damage to bridge structures in Rikuzen-Takada City and the emergency road network recovery actions. In *Proceedings of the International Symposium on Engineering Lessons Learned from the 2011 Great East Japan Earthquake* (pp. 1429–1438).
- Van Ginkel, K. C., Dottori, F., Alfieri, L., Feyen, L., & Koks, E. E. (2021). Flood risk assessment of the European road network. *Natural Hazards and Earth System Sciences*, 21(3), 1011–1027. <https://doi.org/10.5194/nhess-21-1011-2021>
- Vescovo, R., Adriano, B., Mas, E., & Koshimura, S. (2023). Beyond tsunami fragility functions: Experimental assessment for building damage estimation. *Scientific Reports*, 13(1), 14337. <https://doi.org/10.1038/s41598-023-41047-y>
- Williams, J. H., Wilson, T. M., Horspool, N., Lane, E. M., Hughes, M. W., Davies, T., Le, L., & Scheele, F. (2019). Tsunami impact assessment: Development of vulnerability matrix for critical infrastructure and application to Christchurch, New Zealand. *Natural Hazards*, 96(3), 1167–1211. <https://doi.org/10.1007/s11069-019-03603-6>
- Williams, J. H., Wilson, T. M., Horspool, N., Paulik, R., Wotherspoon, L., Lane, E. M., & Hughes, M. W. (2020). Assessing transportation vulnerability to tsunamis: Utilising post-event field data from the 2011 Tohoku tsunami, Japan, and the 2015 Illapel tsunami, Chile. *Natural Hazards and Earth System Sciences*, 20(2), 451–470. <https://doi.org/10.5194/nhess-20-451-2020>
- Yamashita, K., Sugawara, D., Takahashi, T., Imamura, F., Saito, Y., Imato, Y., ... Nishikawa, A. (2016). Numerical simulations of large-scale sediment transport caused by the 2011 Tohoku Earthquake Tsunami in Hirota Bay, Southern Sanriku Coast. *Coastal Engineering Journal*, 58(4), Article 1640015. <https://doi.org/10.1142/S0578563416400155>
- Yamashita, K., Yamazaki, Y., Bai, Y., Takahashi, T., Imamura, F., & Cheung, K. F. (2022). Modeling of sediment transport in rapidly-varying flow for coastal morphological changes caused by tsunamis. *Marine Geology*, 449, Article 106823. <https://doi.org/10.1016/j.margeo.2022.106823>
- Zhu, Z., Gou, L., Liu, S., & Peng, D. (2023). Effect of urban neighbourhood layout on the flood intrusion rate of residential buildings and associated risk for pedestrians. *Sustainable Cities and Society*, 92, Article 104485. <https://doi.org/10.1016/j.scs.2023.104485>